Electronic Supplementary Material (ESI) for Journal of Materials Chemistry A.

An Effective Integrated Cu_2O Photocathode to Boost Photoeletrocatalytic CO_2 Conversion

Yongjian Jia[1,2*], *Zenghua Tian*[1,2] ，*Jingyu Gao*[1,2],

1. *National Engineering Research Center for Technology and Equipment of Environmental Deposition, Lanzhou Jiaotong University, Lanzhou 730070, China;*
2. *Key Lab of Opt-Electronic Technology and Intelligent Control of Ministry of Education, Lanzhou Jiaotong University, Lanzhou 730070, China;*

1. Materials and characterizations.

All chemicals were analytical grade and were used as received. Solutions were prepared using high purity water (Millipore Milli-Q purification system, resistivity > 18 MΩ·cm). The fluorine-doped tin oxide (FTO) conductive glass was purchased from Nippon Sheet Glass Company (Japan) and was ultrasonic cleaned with acetone, ethanol and deionized water for 20 min each in sequence prior to use. CO_2 gas and N_2 gas were of super grade purity (99.999%) from Lanzhou Yulong Co. Ltd. $^{13}CO_2$ was 99% enriched, and provided by Sigma-Aldrich.

The obtained samples were characterized by X-ray powder diffraction (XRD) on a Rigaku D/Max-2500/PC powder diffractometer using Cu Kα radiation (operating voltage: 40 kV, operating current: 200 mA, scan rate: 5° min^{-1}). The morphologies of the electrodes were performed by a Quanta 200 FEG scanning electron microscope (SEM) equipped with an energy dispersive spectrometer (accelerating voltage of 20 kV). X-ray photoelectron spectroscopy (XPS) measurements were performed by Thermo ESCALAB 250Xi with monochromatized Al Kα excitation.

2. Preparation of Photocathodes

2.1 Synthesis of Polystyrene Spheres (PS)

Monodispersed polystyrene (PS) beads were synthesized by emulsion polymerization reaction [S1]. Typically, 5 ml styrene monomer and 1.5 g of polyvinylpyrrolidone (PVP ~55000 Mw) were added to the 135 mL of ethanol in three neck 500ml round bottom flask. The reaction mixture was deoxygenated by bubbling nitrogen gas through it at 70 ^{o}C under constant stirring. After 30 min, 78 mg of AIBA was dissolved in deionized water (15 mL) was added to the above mixture, and was polymerized at same temperature for 20 hrs to obtain PS beads. The PS beads was collected and washed with ethanol for three time and redispersed in 40ml of ethanol to fabricate 3D opal structures. Finally, the size of PS beads was determined to 400 nm by SEM (**Figure S9**).

2.2 Synthesis of FeOOH Film

FeOOH was first deposited on the FTO-coated glass substrates (TEC-7) *via* an aqueous chemical growth [S2, S3]: FTO substrates were immersed in an aqueous solution containing 0.15 M $FeCl_3 \cdot 6H_2O$ and 1 M Na_2SO_4, then heated at 100 °C for about 2 h. Subsequently, the samples were thoroughly washed with water, followed by drying at room temperature.

2.3 Synthesis of PS Films

The PS bead solutions were diluted from their stock solutions to 0.15Wt%. The water was used consistently as the solvent for the PS bead deposition.

The substrates (1×2 cm^2 FTO) were set tilted at a 60 angle with each sample placed individually in small vials. 1.5 mL of the desired PS bead solution was carefully dispensed into the vials.

After the deposition, the films with bead sizes ~400 nm were immersed in ethanol for 1 h, and then removed and carefully dried using a gentle stream of nitrogen on the back side of the substrate.

2.4 Synthesis of *p*-Cu_2O Films

p-Cu_2O was synthesized with electrodeposition by adapting a previously reported procedure[S4]. In a typical experiment, 0.4 M copper sulfate pentahydrate solution was used as the plating solution, prepared by stirring 4.99 g $CuSO_4 \cdot 5H_2O$ (Sigma-Aldrich, ≥98%) in 50 ml of Millipore water. Lactic acid (3 M, 13.51 g, Sigma-Aldrich, 85%) was added to stabilize Cu^{2+} in basic solution, and then 3M NaOH (Sigma-Aldrich, ≥98%) was added to the solution until the pH of the plating solution reached 12.0. Cu_2O was deposited on the substrate with a constant current density: -0.1 mA cm^{-2} in a three-electrode configuration under room temperature for 2.5 h. After deposition, the samples were gently rinsed with water and then gently dried with a nitrogen gun.

2.5 Synthesis of Polypyrrole (PPy)

The work electrode was immersed in an acetonitrile/ dichloromethane (3:1) solution containing pyrrole (3×10^{-3} M) and TBAP (0.1 M). The electropolymerization was conducted in a three-electrode system at room temperature for 60 min at a constantly applied voltage of 1.2 V *vs* Ag/Ag^+. Subsequently, the PPy film was rinsed by acetonitrile and ethanol several times and then dried under argon [S5].

2.6 Preparation of Inver Opal Structure

The electrode containing PS beads were removed by cycling DMF rinses to yield porous substrates. Subsequently, the film was rinsed by water several times and then dried under argon [S6].

3. PEC-CO_2 Reduction Reaction

The PEC test was conducted in a single-compartment, three-electrode electrochemical cell with a potentiostat (CHI660D), under simulated AM 1.5G solar light irradiation (100 mW cm^{-2}). Before the CO_2 reaction, 0.1 M Bu_4NPF_6 electrolyte in the AcNE was saturated by bubbling CO_2 gas for at least 30 min, and the CO_2 inlet flow rates kept constant at 30 mL/min.

The surface area of electrode was 0.9×0.9 cm^2.

The recorded potentials versus Ag/Ag^+ converted to the potential *vs* Fc^+/Fc on account of the following equation:

$$E\left(vs\ Fc/Fc+\right) = E(vs\ Ag/Ag+) - 0.19 \qquad (S1)$$

The photocurrent was measured by linear sweep voltammetry with a scan rate of 10 mV s^{-1}. The light irradiation came from the back side of the electrodes for all cases. OCP measurements were performed under open circuit conditions. Mott–Schottky (MS) analysis was carried out at a D.C. potential range of 0.8 to -0.1 V versus Fc^+/Fc with an A.C. potential frequency of 100 Hz in 0.1 M Bu_4NPF_6 under dark conditions.

4. The Two-electrode Cell

The system was conducted in a single-compartment, two-electrode electrochemical cell with three dry batteries (3×1.5V), under simulated AM 1.5G solar light irradiation (100 mW cm^{-2}). Before the CO_2 reaction, 0.1 M Bu_4NPF_6 electrolyte in the AcNE was saturated by bubbling CO_2 gas for at least 30 min, and the CO_2 inlet flow rates kept constant at 30 mL/min.

5. PEC-CO_2RR Product Analysis

The gas products were analyzed by gas chromatography (GC-2060, Ruimin) equipped with a flame ionization detector (FID) to detecting CO. The CO_2 gas was continuously purged at an average rate of 30 mL/min. Nitrogen was used as the carrier gas.

The ***Faradaic Efficiency*** of the gas compound (FE) can be calculated by the following equation:

$$FE(\%) = \frac{n \times C \times u \times F}{I \times V_m} \times 100\% \tag{S2}$$

where I is the total current density, n is electrons transferred for gas reduction product (CO), u is outlet gas flowrate (30 mL/min), V_m is molar volume (22.4 L/mol), F is the Faraday constant (96485 C/mol), C is volume fraction of the reduction product (CO) detected by GC.

Quantum Efficiency

The 2 electrons reduction process from CO_2 to CO, the overall quantum efficiency (QE) of the process was determined by using the following equation:

$$\text{QE} = \frac{\text{Number of CO molecules} \times 2}{\text{Number of incident photons}} \times 100\%$$

Number of incident photons=

$$\frac{\text{absorbed light flux}\left(\frac{\text{mW}}{\text{cm}^2}\right) * \text{suface area}\left(\text{cm}^2\right) * \text{radiation time(s)}}{\text{each photo engergy (J)} * 6.02\times10^{23}}$$

Each photo energy: E=hc/λ

Planck's constant $h = 6.626 \times 10^{-34}$ J·s, $c = 3 \times 10^{8}$ m/s, $\lambda \cong 500$ nm

The half-cell solar-to-CO efficiency **(**$\eta_{STC)}$ was calculated using the following equation [S11]:

$$\eta_{stc} = \frac{J(mA/cm^2 \times FE_{CO}(\%) \times (1.34 - V_{bias})(V))}{P_{in}(mW/cm^2)}$$

where *J* is the photocurrent density, and *FE* is the Faradaic efficiency towards CO, E is the applied potential *vs.* RHE, P is the light power density, and 1.34 V is the thermodynamic potential for CO_2 reduction to CO at 25°C.

6. The Charge Separation and Injection Efficiency

In principle, the photocurrent of CO_2 redcution ($J_{photocurrent}$) is a product of the rate of photon absorption expressed as a current density ($J_{absorbed}$), the charge separation yield of the photogenerated carriers ($P_{charge\ separation}$), and charge injection yield to the electrolyte ($P_{charge\ injection}$):

$$J_{photocurrent} = J_{absorbed} * P_{charge\ separation} * P_{charge\ injection} \quad \text{(S3)}$$

The photocurrent measured in the electrolyte with TEOA ($J^{TEOA}{}_{photocurrent}$) is only a product of $J_{absorbed}$ and $P_{charge\ separation}$, assuming the charge injection yield becomes 100% ($P_{charge\ injection} = 1$) in the presence of a hole scavenger (TEOA) in the electrolyte:

$$J^{TEOA}{}_{photocurrent} = J_{absorbed} * P_{charge\ separation} \quad \text{(S4)}$$

Based on equation (1) and (2), the charge injection yield can be achieved:

$$P_{charge\ injection} = J_{\ photocurrent} / J^{TEOA}{}_{photocurrent} \quad \text{(S5)}$$

The charge separation yield is given by:

$$P_{charge\ separation} = J^{TEOA}{}_{photocurrent} / J_{absorbed} \quad \text{(S6)}$$

Assuming complete absorption and 100% utilization of band gap photons of Cu_2O, a photocurrent of 12.9 mA cm^{-2} is theoretically possible under standard AM 1.5G solar illumination (J_{Cu2O} absorbed). Thus, the charge separation and injection efficiency of photoelectrodes can be calculated according to equation (3) and (4).

7. Space-charge-limited-current, SCLC

Hole-only diodes were fabricated on FTO coated glass with a PEDOT:PSS or FeOOH bottom contact and a MoO_x/Ag top contact [S7]. The top contact was the injecting electrode in both cases. The semiconducting layer was the blend of polymer (as used in the optimal solar cell devices). The structure of device was exhibited as: ITO/PEDOT:PSS/Polymers (active players)/MoO_3/Ag or ITO/FeOOH/Polymers (active players)/MoO_3/Ag.

Device areas (A) were 0.1 cm^2. The current density, J, as a function of applied electric field, E, displayed space charge limited regimes. The latter was fitted using the following model to extract the zero-field mobility, μ_0, and the field dependence coefficient, γ,

$$J = \frac{9}{8}\varepsilon_0\varepsilon_r\mu_h\frac{E^2}{L^3}$$

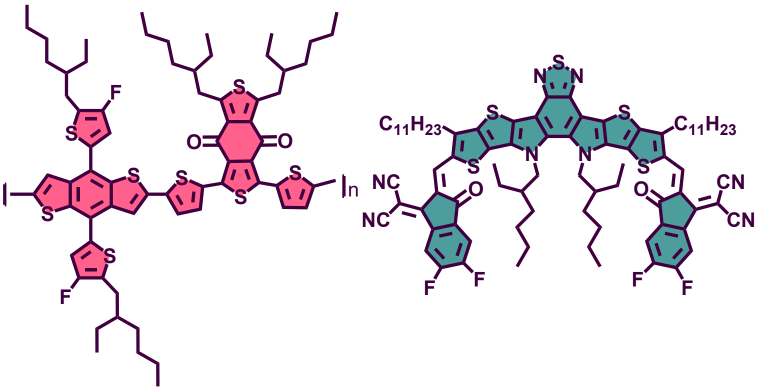

PM6 **Y6**

Figure S1 Molecular Structures of PM6 and Y6

8. The time-resolved photoluminescence (TRPL) curves are fitted with a biexponential function model and the detailed fitted parameters are provided in Table S3. The average carrier lifetime is calculated by the following equation:

$$A_1^* = \frac{A_1 \times \tau_1}{A_1\tau_1 + A_2\tau_2}$$

$$\tau_{avg} = \frac{A_1^*\tau_1^2 + A_2^*\tau_2^2}{A_1\tau_1 + A_2\tau_2}$$

where τ_1 represents fast relaxation and trapping in bulk, τ_2 represents the surface recombination

Table S1 Kinetic analysis of PL decay for samples

Sample	A_1	τ_1 (ns)	A_2	τ_2 (ns)	A_1*(%)	A_2*(%)	τ_{avg} (ns)	k_{ct} (s^{-1})
Cu_2O	1.16	1.27						
FCu	1.1	1.52	0.09	15.49	54.5	45.5	14.0	6455.78[a]
FCu Io	1.1	1.45	0.08	14.09	58.6	41.4	12.5	641.45[b]
FCuP Io	0.9	1.18	0.2	10.04	34.6	65.4	9.52	2862.92[c]

$$k_{ct}\,(Cu_2O \rightarrow FeOOH) = \frac{1}{\tau_2}\left(Cu_2O \rightarrow FeOOH\right) - \frac{1}{\tau_2}(Cu_2O)$$

$$k_{ct}\,(Cu_2O \rightarrow Io) = \frac{1}{\tau_2}\left(Cu_2O \rightarrow Io \rightarrow FeOOH\right) - k_{ct}(Cu_2O \rightarrow FeOOH)$$

$$k_{ct}(Cu_2O \rightarrow PPy) =$$

$$\frac{1}{\tau_2}\left(PPy \leftarrow Cu_2O \rightarrow Io \rightarrow FeOOH\right) - k_{ct}(Cu_2O \rightarrow FeOOH) - k_{ct}(Cu_2O \rightarrow \mathrm{Io})$$

9. Normalized parameter (D)

A normalized parameter (D) is introduced to determine the charge recombination behavior.

$$D = \frac{I_t - I_{st}}{I_{in} - I_{st}}$$

where I_t, I_{st} and I_{in} are the time-dependent, steady-state and initial photocurrent, respectively, as indicated in **Figure 7d**. The transient time constant (k) reflecting the general behavior of charge recombination can be defined as the time when $\ln D = -1$ in the normalized plots of $lnD \sim t$.

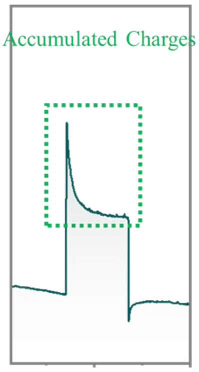

With the light switched on, the transient photocurrent density shown a sharp peak before it exponentially dropped to a steady state. This sharp peak was supposed to be from the accumulated photoinduced charges, which were generated and separated to appear as an electric current in an irradiated photoelectrode but were eventually trapped and unable to reach the surface for the reaction. The accumulated charges can be quantified by integrating the transient photocurrent density minus the steady-state value with respect to time.

10. Ideality factor (*n*$_{ID}$)

n$_{ID}$, the relationship between V_{oc} and P_{light} follows the formula, was calculated according to the following equation:

$$\mathrm{V_{oc}} = \frac{n_{ID} k_B T}{q} \ln(P_{light})$$

Where k_B is the Boltzmann constant, T the thermodynamic temperature, and q the electron charge.

11. The open circuit potential (OCP) transient decay was measured in the open circuit potential model of the electrochemical workstation. The working electrode was first stabilized in 0.5M Na_2SO_4 solution for 30 s under AM 1.5 G, and then the light source was turned off to record the OCP decay curve for the next 100 s. Transient photocurrent was measured at the same experimental conditions.

12. Contact Angle Measurements

The wettability of the samples was determined by measuring the CA of a liquid droplet on the sample surface. The method of digital video image was used to process the sessile droplets by a CA apparatus (LAUDA Scientific, OCA25) in ambient air at room temperature. A CCD camera with space resolution 768×576 and color resolution 256 gray levels was applied to capture the droplet images. A droplet (5 mL) of water or acetonitrile was injected onto the surface with a 1-mL micro-injector. The CA values for each film before or after solar light irradiation for 30 min were averaged from five measurements.

13. Electrochemical Impedance Spectroscopy

According to Peter's article, k_{CT} and k_{trap} are obtained from the EIS fitting results following the below equations:

$$k_{ct} = \frac{1}{\mathrm{R}_{\mathrm{ct}} \times \mathrm{C}_{\mathrm{ct}}}$$

$$k_{ct} = \frac{1}{\mathrm{R}_{trap} \times \mathrm{C}_{trap}}$$

The charge transfer efficiency (Φ_{trans}) for PEC water reduction can be expressed as:

$$\Phi = \frac{\mathrm{k}_{\mathrm{ct}}}{\mathrm{k}_{\mathrm{ct}} + \mathrm{k}_{\mathrm{trap}}}$$

Ref: K. G. Upul Wijayantha, S. Saremi-Yarahmadi and L. M. Peter, Phys. Chem. Chem. Phys. 2011, 13, 5264.

14. Characterization and Results

Table S2 Faradaic Efficiency (%) of *PEC*-CO_2RR Product

Potential *vs* Ag/Ag^+	***p*-Cu_2O**	**FCuP**		**FCuP Io**	
	Under light	Under dark	Under light	Under dark	Under light
− 1.6 V	3.1±0.15	9.9±0.02	19.5±0.98	9.6±0.48	36.4±1.09
− 1.7 V	11.6±0.58	54.2±1.09	57.3±2.86	59.1±2.95	69.1±2.07
− 1.8 V	58.5±2.9	73.8±2.71	72.7±3.64	80.9±4.04	88.9±2.67
− 1.9 V	45.9±2.2	76.5±3.69	90.7±4.53	93.4±4.67	102.3±3.07
− 2.0 V	47.0±2.3	83.8±4.19	101.8±5.09	98.2±5.14	103.2±3.10

Table S3 CO production rate (μmol/h)

Potential *vs* Ag/Ag$^+$	***p*-Cu$_2$O**	**FCuP**		**FCuP Io**	
	Under light	Under dark	Under light	Under dark	Under light
− 1.6 V	0.04±0.001	0.46±0.02	1.10±0.04	0.16±0.01	1.44±0.06
− 1.7 V	0.30±0.01	3.12±0.12	3.36±0.11	3.50±0.14	4.74±0.19
− 1.8 V	4.97±0.19	4.49±0.17	9.12±0.36	11.70±0.46	13.01±0.52
− 1.9 V	6.49±0.26	8.06±0.32	21.6±0.86	24.04±0.96	24.09±0.96
− 2.0 V	8.74±0.34	9.13±0.36	24.6±0.98	33.20±1.32	46.17±1.84

Table S4 Quantum Efficiency (%)

Potential *vs* Ag/Ag^+	***p*-Cu_2O**	**FCuP**	**FCuP Io**
– 1.6 V	0.003	0.07	0.09
– 1.7 V	0.023	0.18	0.31
– 1.8 V	0.33	0.61	0.86
– 1.9 V	0.43	1.44	1.60
– 2.0 V	0.58	1.64	3.06

Table S5 Solar-to-CO (η_{STC}) efficiencies for 1 h under AM 1.5G illumination

Potential *vs* Ag/Ag$^+$	***p*-Cu$_2$O**	**FCuP**	**FCuP Io**
– 1.6 V	0.003	0.07	0.09
– 1.7 V	0.02	0.15	0.24
– 1.8 V	0.24	0.41	0.66
– 1.9 V	0.27	0.89	0.99
– 2.0 V	0.30	0.86	1.58

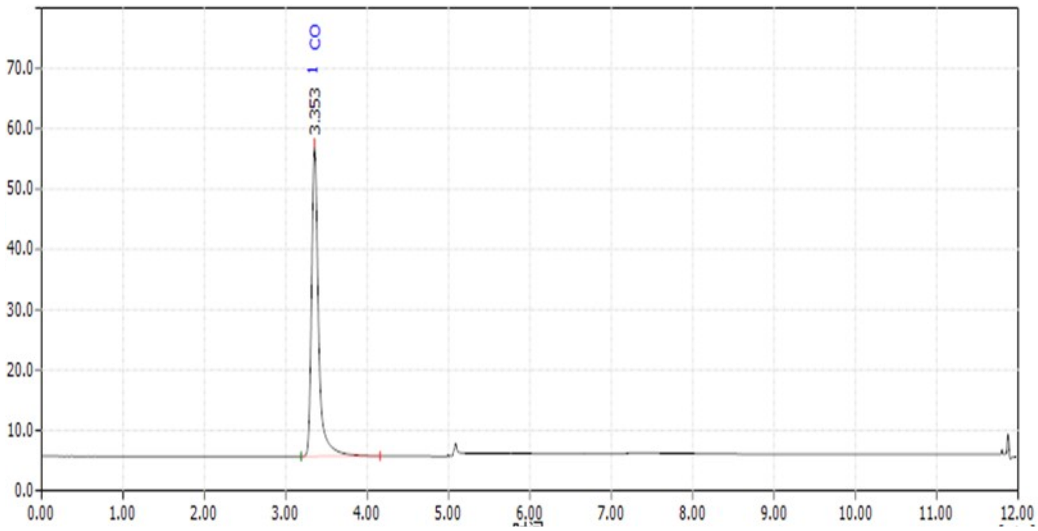

Figure S2 Raw GC data: The CO signal from CO_2 reduction by FID channel

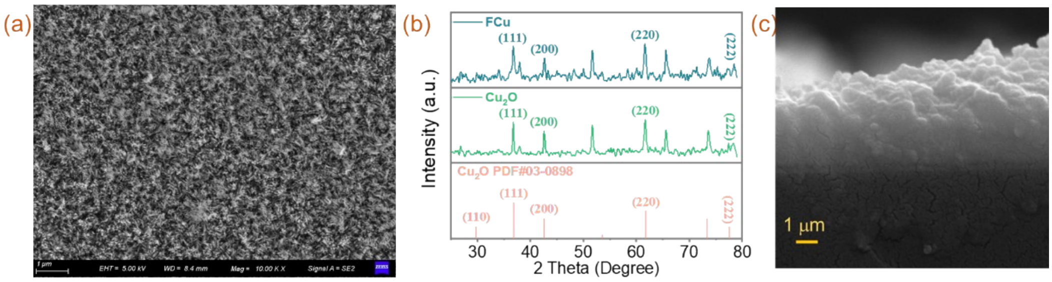

Figure S3 (a)Top-view SEM image of FeOOH, (b)XRD refinement of Cu_2O and FCu photocathodes, (c) Cross-sectional SEM image for FCu photocathode

Table S6 The slow photo effect on the Cu_2O Io based photocathodes

Sample	Without light	With light
Cu_2O Io		
FCuP Io		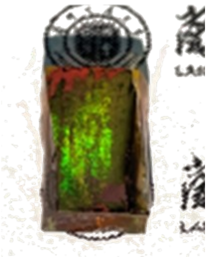

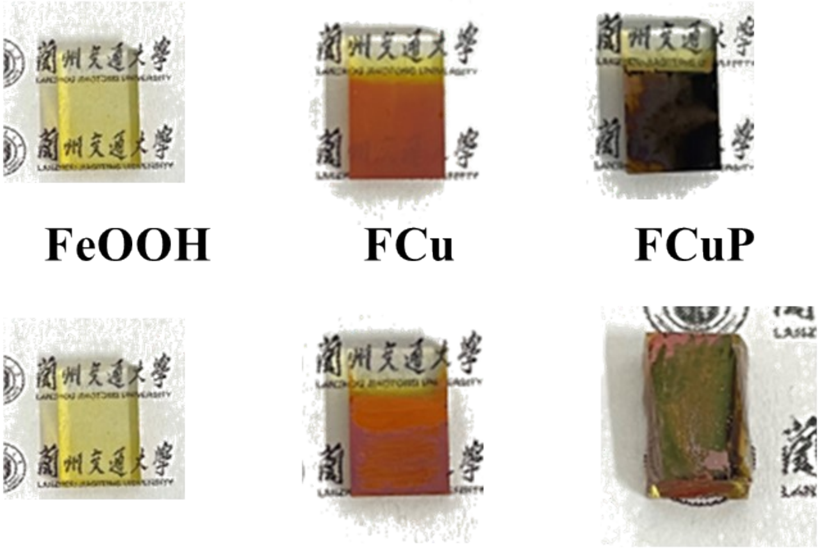

FeOOH FCu FCuP

FeOOH FCuIo FCuPIo

Figure S4 The image of each photocathode

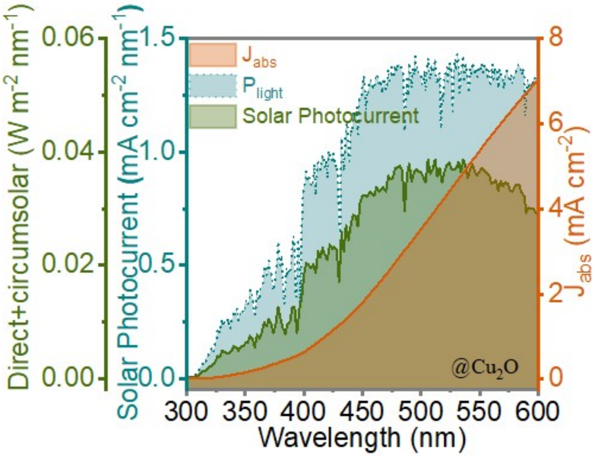

Figure S5 The integrated maximum photocurrent (*J_{abs}*) of Cu_2O photocathodes based on the UV-vis DRS spectra

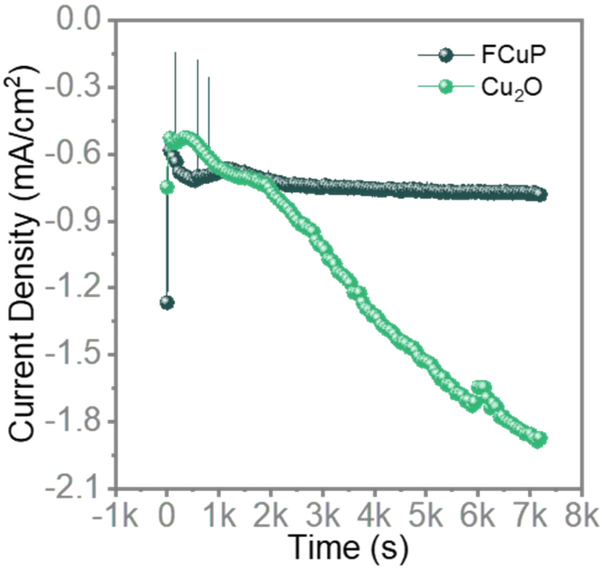

Figure S6 Longtime stability of Chronoamperometry under AM 1.5G simulated sunlight,

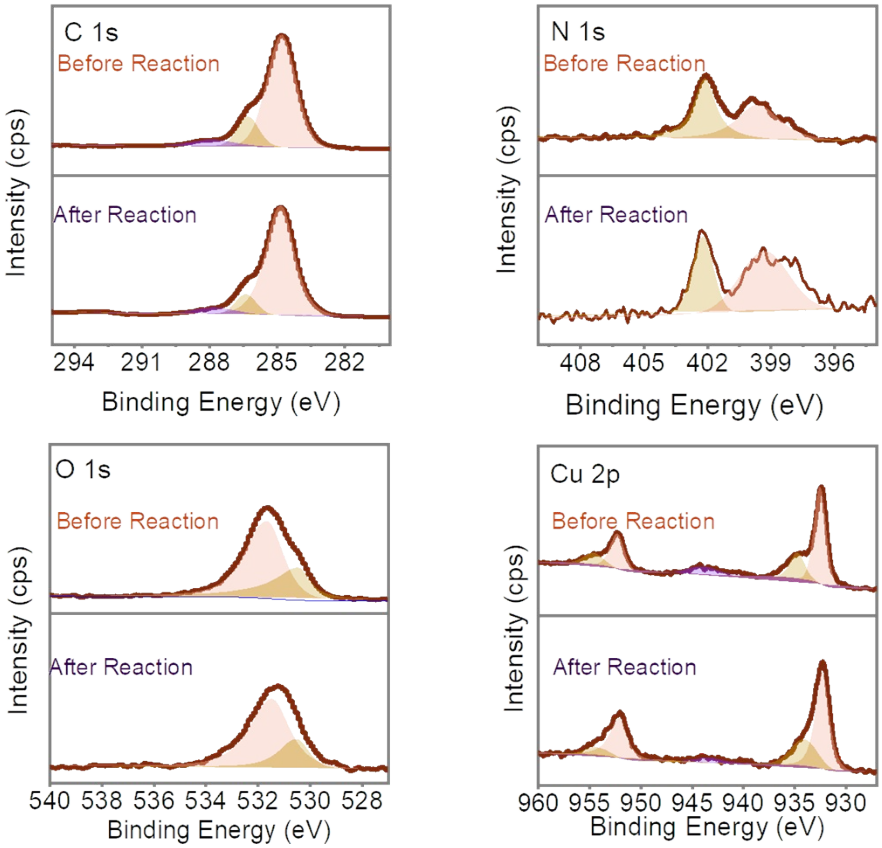

Figure S7 The XPS for FCuP photocathodes before and after PEC CO_2 reaction

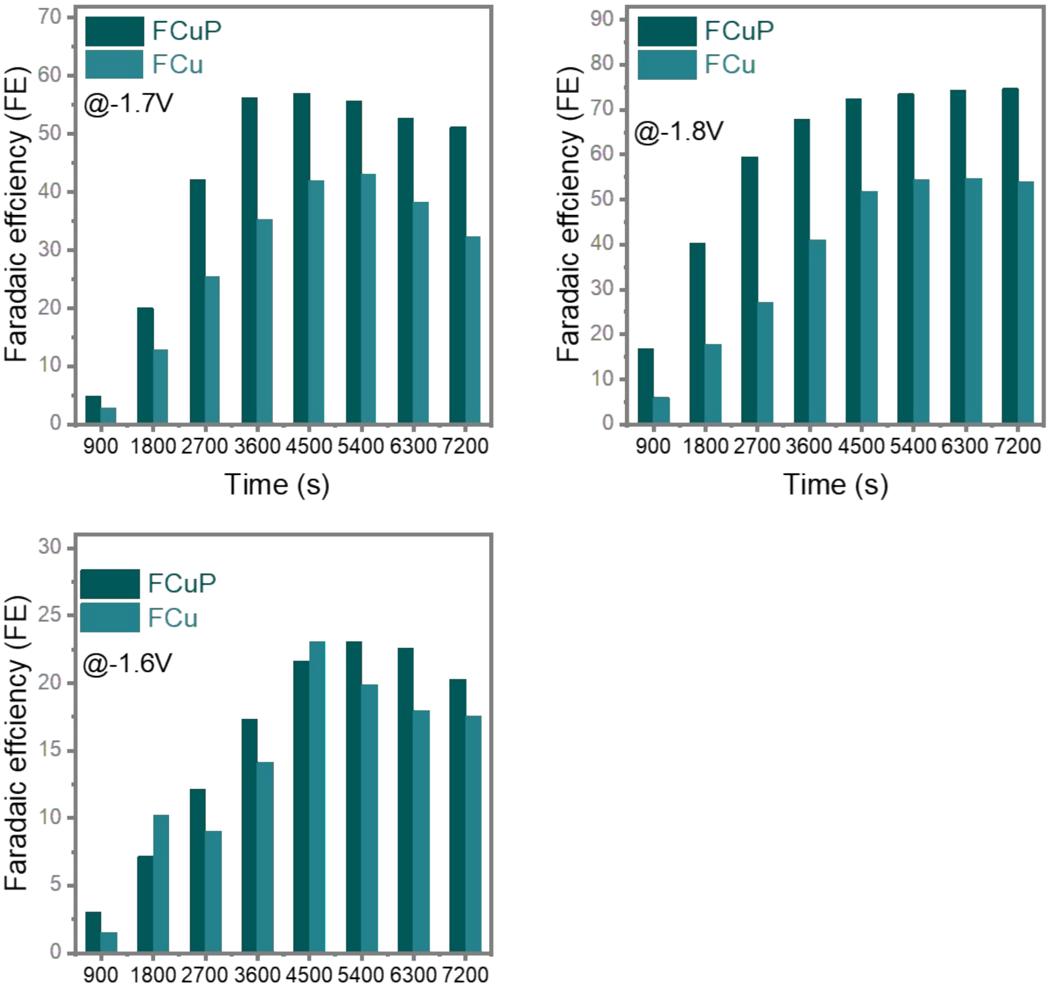

Figure S8 Instants FEs for the two cathodes under dark at −1.6V, −1.7V and −1.8V vs Ag/Ag$^+$

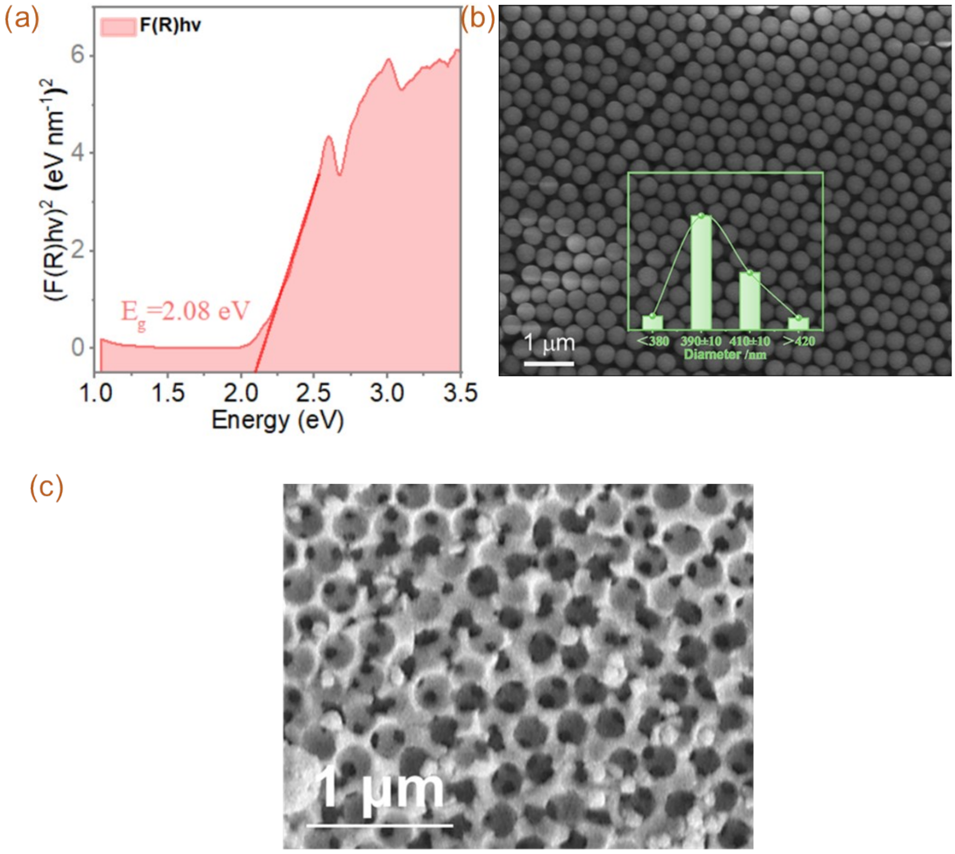

Figure S9 (a) Tauc plots of Cu_2O for band gap calculation based on UV-vis-IR diffuse reflectance spectra (b) SEM and diameter of PS beads and (c) Top-view SEM image for Cu_2O Io

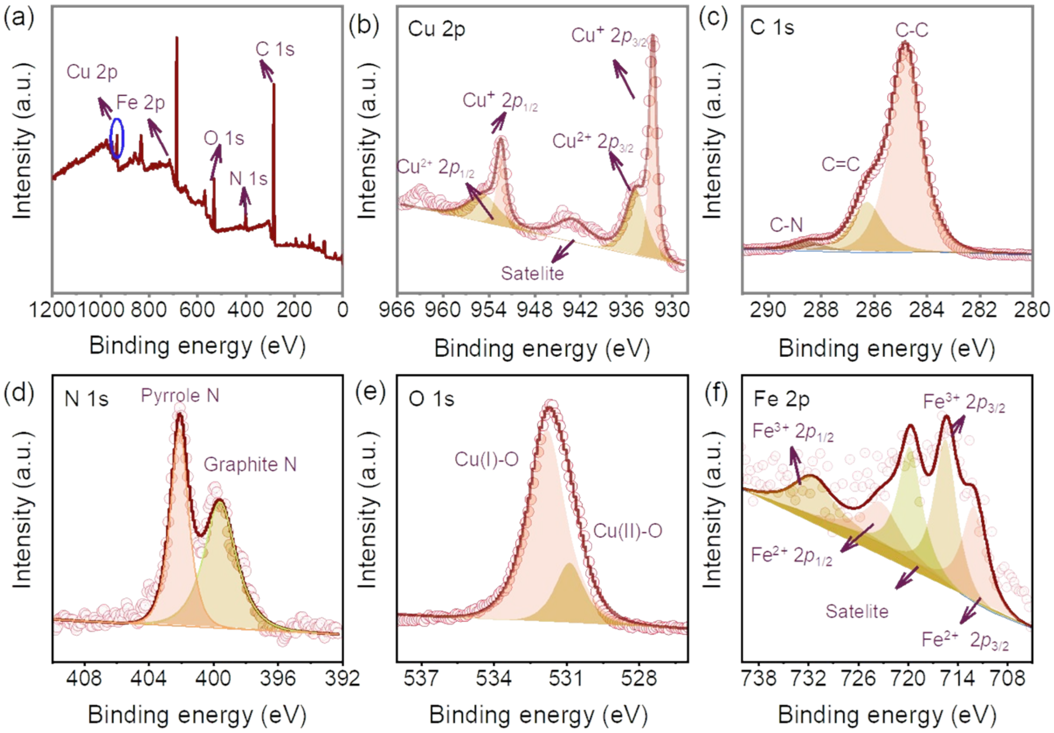

Figure S10 High-resolution XPS for FCuP Io photocathode

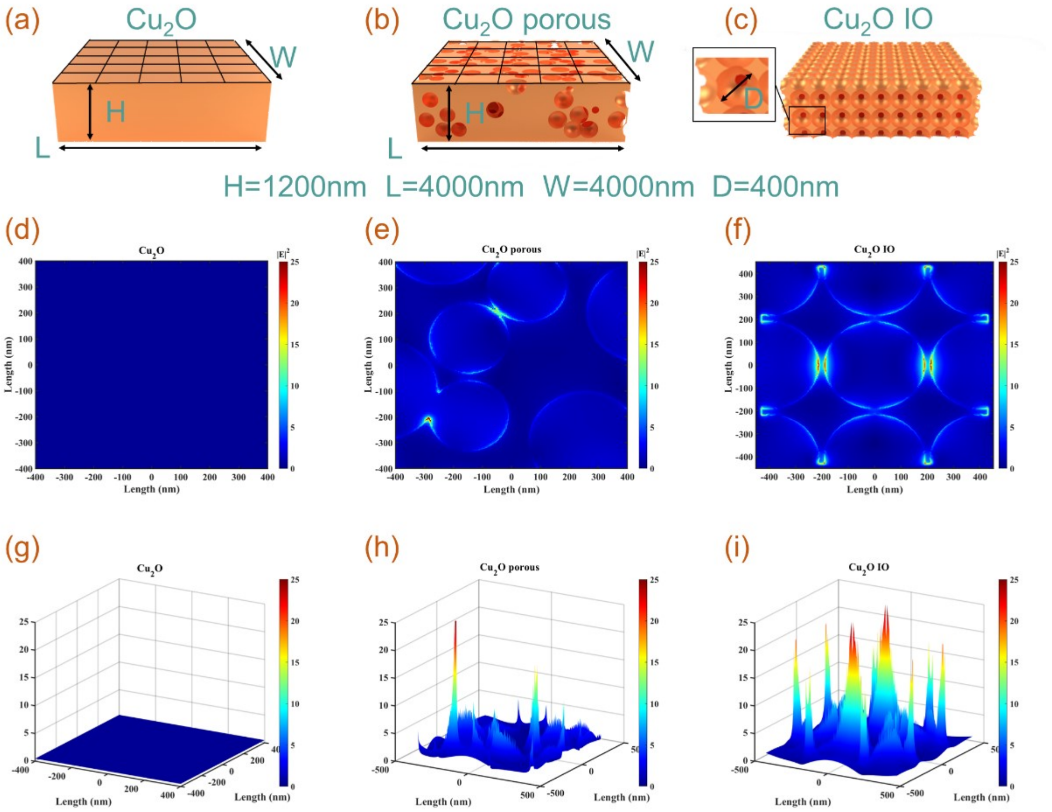

Figure S11 Spatial distribution of the electric field for planar Cu_2O, (b) disordered porous Cu_2O and (c) three-dimensional array Cu_2O; 2D and 3D color coded electric field distributions (d, g) planar Cu_2O, (e, h) disordered porous Cu_2O and (f, i) three-dimensional array Cu_2O. The incident linear polarized light wavelength is 500 nm

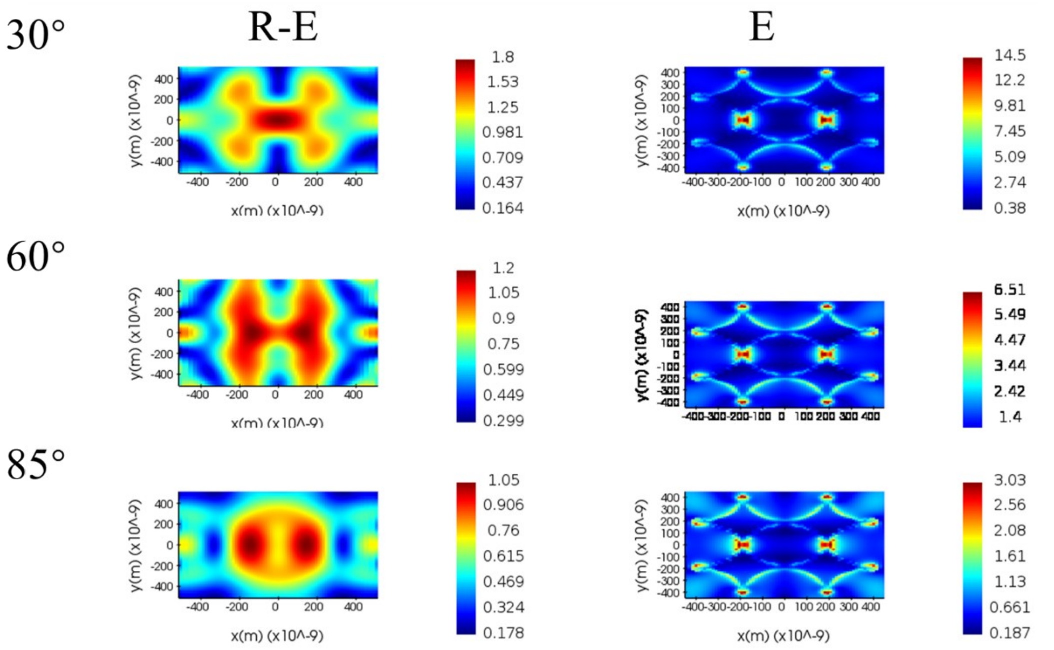

Figure S12 Schematic diagrams and 2D color coded reflected electric field distributions and electric field distributions for the Cu_2O Io as a function of the tilt angle of the incident light, 30^{o}, (b) 60^{o} and (c) 85^{o}. The incident linear polarized light wavelength is 500 nm.

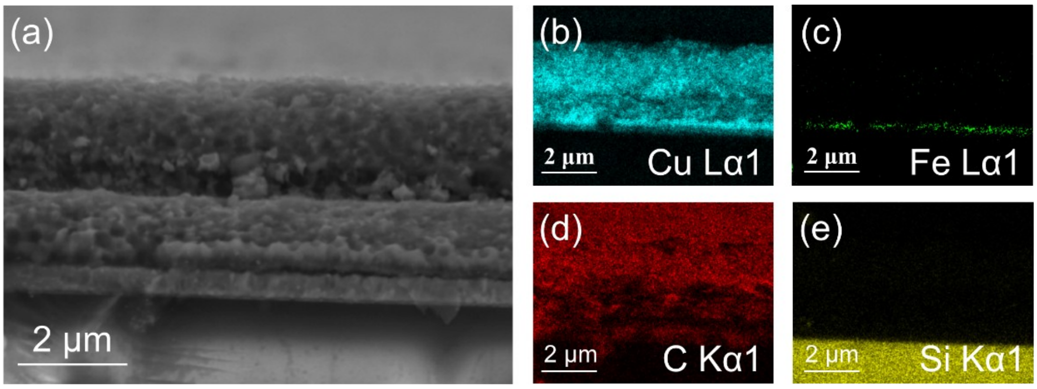

Figure S13 The cross-section SEM and images and mapping for FCuP Io photocathode

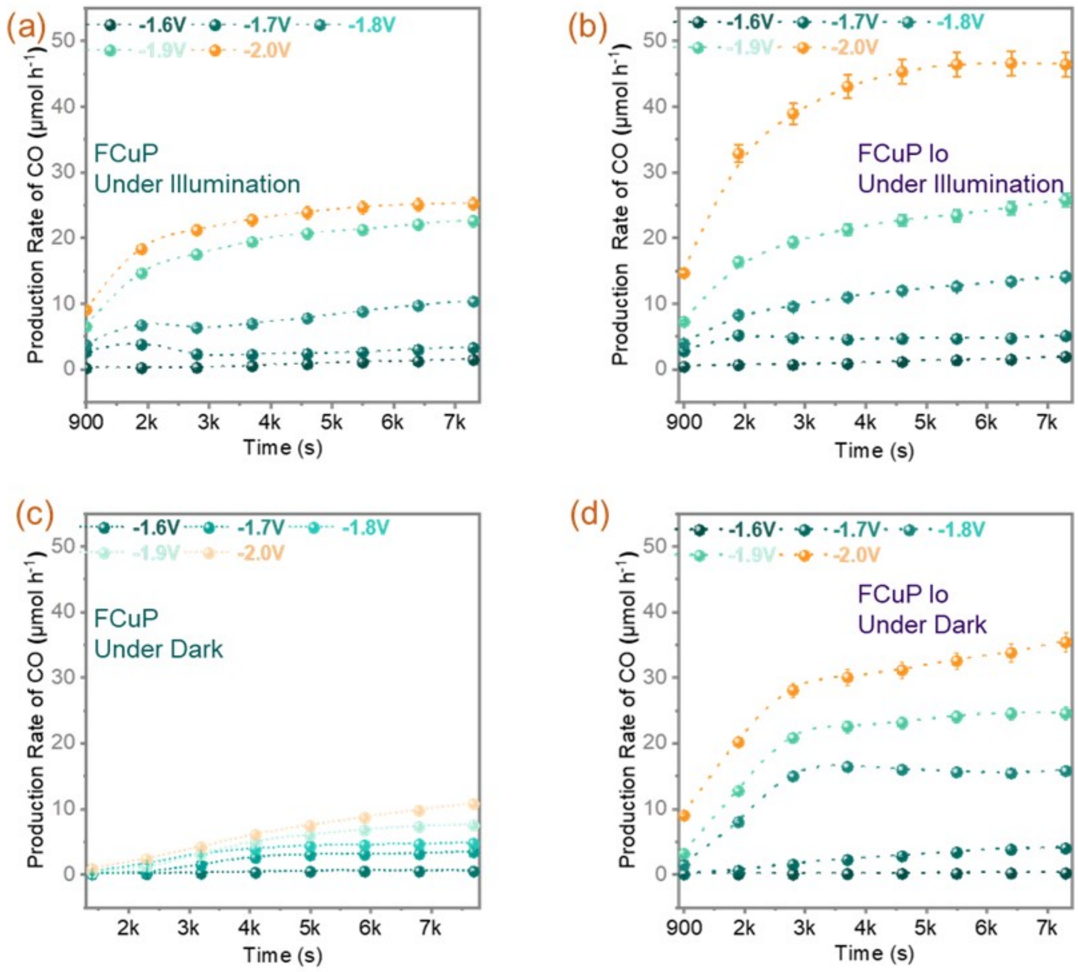

Figure S14 Instantaneous production rate of CO for FCuP and FCuP Io photocathodes with or without AM 1.5G illumination

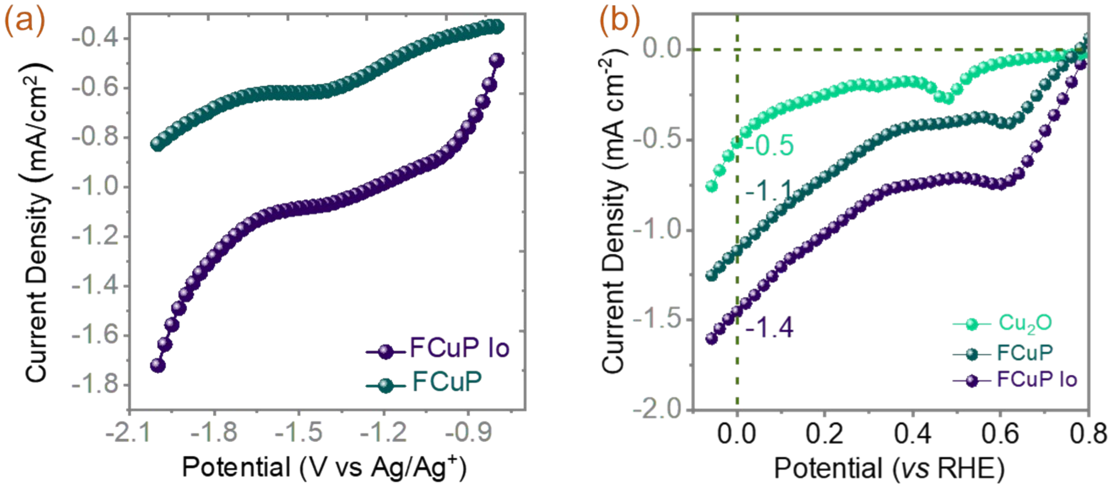

Figure S15 (a) Current density for FCuP Io and FCuP cathodes under dark, (b) Current-potential curves of the three photocathodes under illumination

$$FF = \frac{J_{max} \times V_{max}}{J_{sc} \times V_{oc}}$$

Where J_{max} and V_{max} are the photocurrent density and the potential corresponding to the optimal ABPE, J_{sc} is the photocurrent density at 0V, and V_{oc} is the photocurrent onset potential.

Sample	J_{max}	V_{max}	J_{sc}	V_{oc}	**FF**
Cu_2O	0.17	0.47	0.5	0.65	0.24
FCuP	0.42	0.62	1.1	0.76	0.31
FCuP Io	0.75	0.62	1.4	0.74	0.47

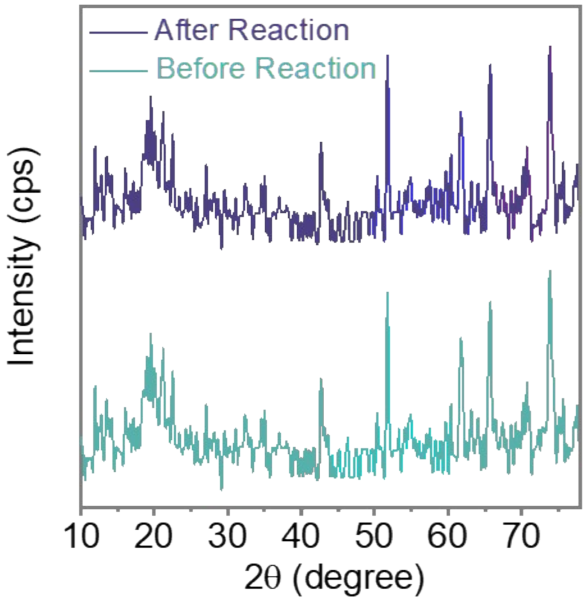

Figure S16 The XRD patterns for FCuP Io photocathodes before and after reaction

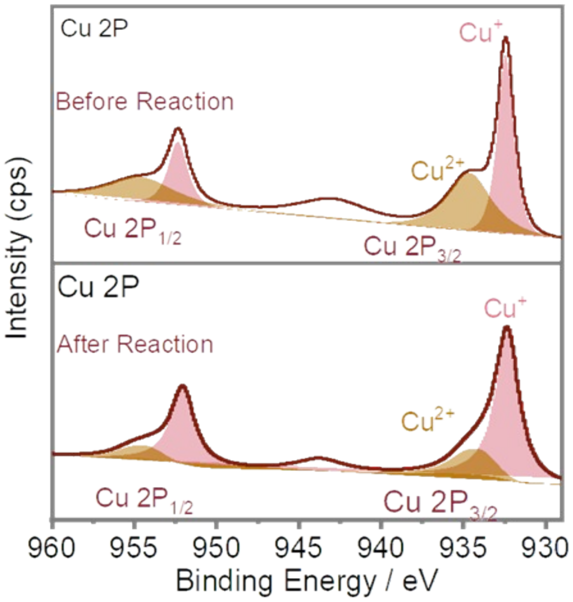

Figure S17 The XPS for FCuP Io photocathodes before and after PEC CO_2 reaction

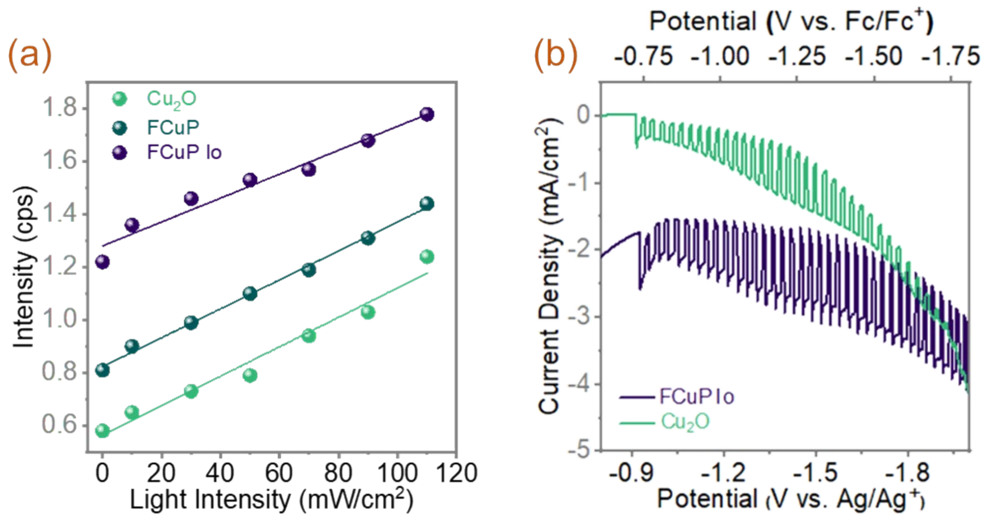

Figure S18 (a) Light intensity dependence of observed photocurrent and (b) Linear sweep voltammetry of the photoelectrodes under chopped visible light

As revealed in **Figure S18a**, a linear dependence on incident light intensity was observed for this system, indicating that a majority of the charges generated in the photoelectrode are being extracted [S12].

The photocurrents can be ascribed to the transfer of photo-induced charges to electrode. As revealed in **Figure S18b**, the photocurrent response of **FCP Io** photoelectrode is dramatically higher than that of bare **Cu_2O**. The enhanced photocurrent response of **FCuP Io** photocathode facilitate the separation and transfer of photogenerated charge carriers, ascribing to the synergistic effect of FeOOH, Cu_2O Io and PPy.

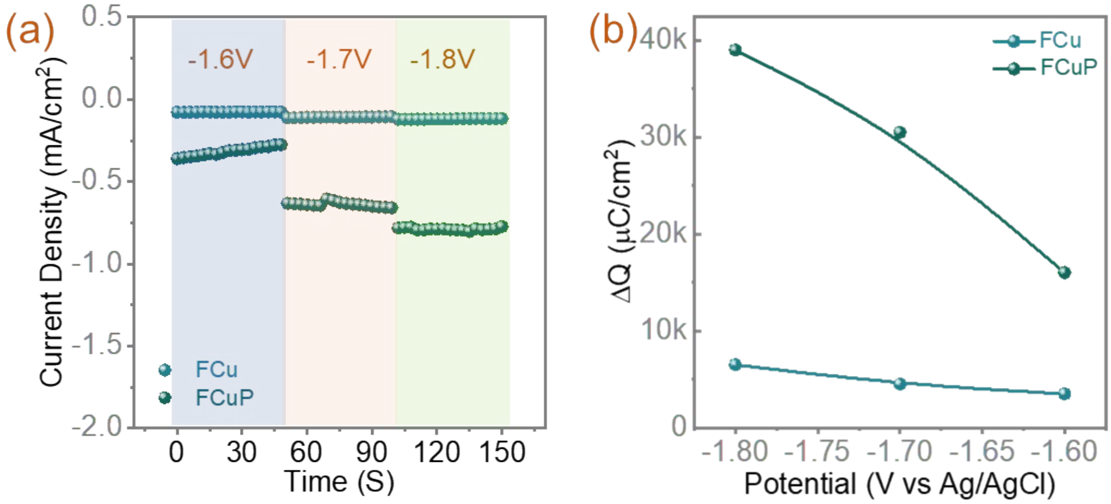

Figure S19 Charge Storage versus Potentials.

The amount of charge storage can be therefore qualitatively determined by the charged passed during the surface recombination process. As **Figure S19** shown, the charge storage capacity of Cu_2O is increased due to the introduction of PPy, denoting that the PPy layer is served as a more efficient ETL for electron transport and storage [S23].

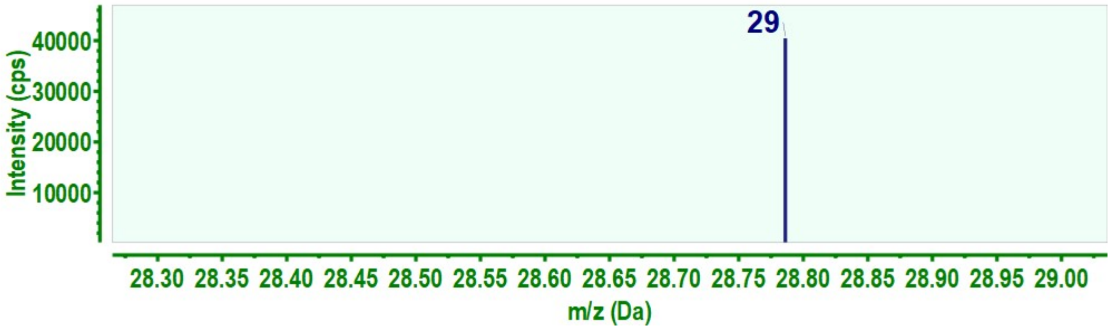

Figure S20 GC-MS analysis ofcarbon products in PEC $^{13}CO_2$ reduction.

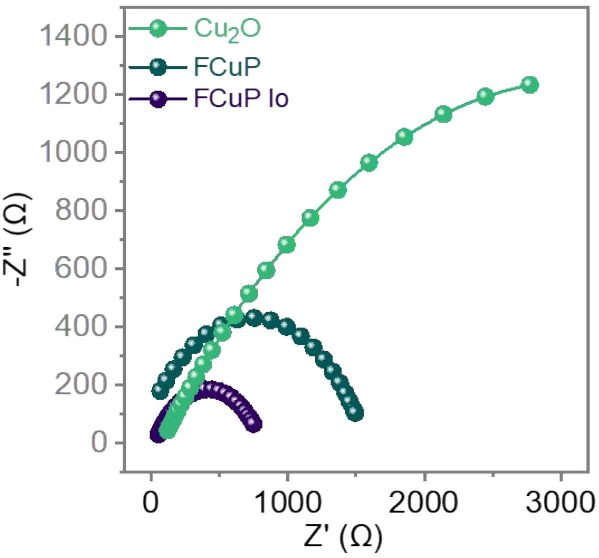

Figure S21 The Nyquist plots for the photocathodes

The impedance arc diameter of the prepared **FCuP Io** photocathode was smaller than two other photocathodes, indicating that the photocathode has a lower resistance in the electron transfer process and acquires enough electrons for CO_2 conversion.

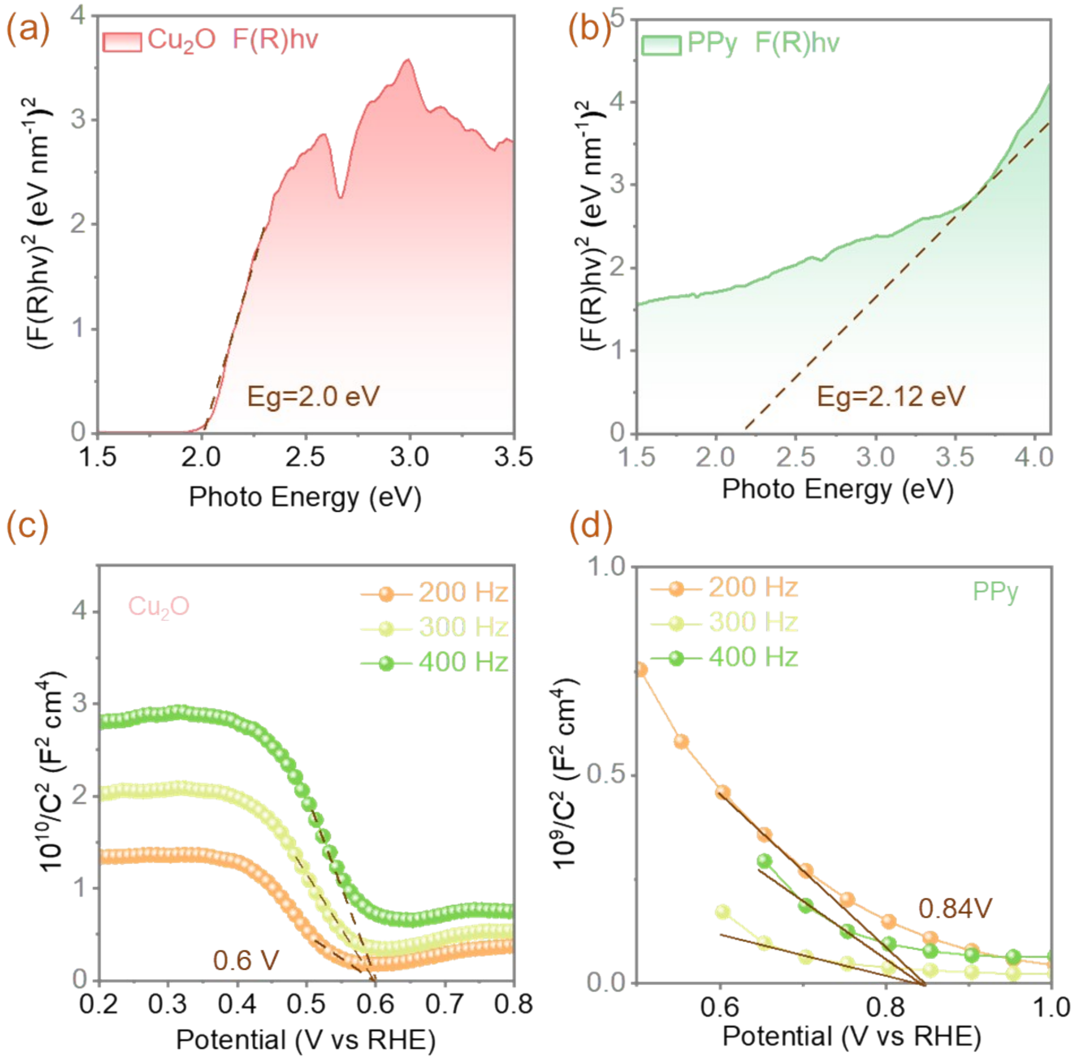

Figure S22 Kubelka-Munk plots (a-b), Mott-Schottky curves (c-d) for p-Cu_2O and PPy films

Table S7 The state-of-the-art performance for the PEC CO_2 conversion over Cu_2O-based photocathodes

Photocathode	**Electrolyte Solution**	**Reactor Configuration**	**FE %**	**Applied Potential**	**Product**	**Yeild**	**Ref**
Si/ZnO/Cu_2O	Na_2CO_3	Single compartment	60	0 *vs.* RHE	Ethanol	–	**S8**
Cu_2O/TiO_2-Cu^+	K_2CO_3	Single compartment	56.5	0.3 V *vs.* RHE	Methanol	～1.02 μmol cm^{-2} h^{-1}	**S9**
Fe_2O_3/WO_3/Au/Cu_2O/Ag	MeCN/Bu_4NPF_6	Single compartment	～60	-1.2 V *vs.* Fc/Fc^+	C_2H_4	N.A.	**S10**
$Cu_3(BTC)_2$/Cu_2O	MeCN/Bu_4NPF_6	H-type cell	95	-1.77 V *vs.* Fc/Fc^+	CO	～15.5 μmol η_{STC}=0.87%	**S11**
Au@Cu_2O@Al:ZnO@TiO_2@Re(bpy)$(CO)_3$Cl	MeCN/Bu_4NPF_6	Single compartment	80-95	-2.05 V *vs.* Fc/Fc^+	CO		**S12**
Cu_2O/5 nm TiO_2	$KHCO_3$	Single compartment	～90	0.4 V *vs.* RHE	Methanol	–	**S13**
Cu_2O/$CuFeO_2$	$KHCO_3$		21.6	0.35 V *vs.* RHE	Formate	–	**S14**

			68.6		Acetate		
Cu_2O-SnO_x	$NaHCO_3$	H-type cell	90.32%（CO～74%;H_2～16%）	-0.35 V *vs.* RHE	CO	η_{STC}=0.06%	**S15**
FCuP Io	MeCN/Bu_4NPF_6	Single compartment	>99	-2.0 V *vs.* Ag/Ag^+ (-1.81 V *vs.* Fc/Fc^+)	CO	46.17μmol h^{-1} (η_{STC}=1.6% & Φ_{QE}=3.0%)	**This work**

Table S8 The state-of-the-art performance for the PEC-CO_2 to CO

Photocathode	Electrolyte Solution	Reactor Configuration	FE %	Applied Potential	Product	Yeild	Ref
poly-RuRe/ NiO	$NaHCO_3$	Single compartment	85	-0.7 V *vs* Ag/AgCl	CO	0.507μmol (5h)	**S16**
Mn-MeCN/MWVNTs	0.1 M $K_2B_4O_7$ + 0.2 M K_2SO_4	Single compartment	80	-1.03 V *vs* Ag/AgCl	CO	325μmol (4h)	**S17**
Co-polypyridyl/SiPL	MeCN + MeOH(10wt%) (0.1 M Bu_4NPF_6)	Single compartment	94	−1.5V *vs.* NHE	CO	η_{STC}=0.19%	**S18**
Si/mesoTiO_2/CotpyP	MeCN+MeOH (10wt%) as electrolyte (0.1 mol/L Bu_4NPF_6)	H-type cell	～50	-1.0 V *vs.* Fc/Fc+	CO	～5 μmol cm^{-2}(8h) η_{STC}=0.04%	**S19**
RuRe/NiO	5:1 DMF-TEA + Et_4NBF	Single compartment	71	-1.2V *vs.* Ag/$AgNO_3$	CO	η_{STC}=0.05%-	**S20**

Au/TiO_2/n^+p-Si	$KHCO_3$		86	−0.8 V *vs* RHE	CO		**S21**
Pt-TiO_2/GaN/n^+-p Si	$KHCO_3$	Single compartment	78	0.17 V *vs* RHE	CO	η_{STC} = 0.87%	**S22**
FCuP Io	MeCN/Bu_4NPF_6	Single compartment	>99	-2.0 V vs. Ag/Ag^+ (-1.77 V vs. Fc/Fc^+)	CO	46.17μmol h^{-1} (η_{STC}=1.6% & Φ_{QE}=3.0%)	**This work**

Reference

[S1] Boppella R., Kochuveedu S. T., Kim H., Jeong M., Mota F., Park J., Kim D. Plasmon-Sensitized Graphene/TiO_2 Inverse Opal Nanostructures with Enhanced Charge Collection Efficiency for Water Splitting. ACS Appl. Mater. Interfaces 2017, 9, 7075−7083.

[S2] Vayssieres, L., Beermann, N., Lindquist, S.-E., Hagfeldt, A. Controlled Aqueous Chemical Growth of Oriented Three-Dimensional Crystalline Nanorod Arrays: Application to Iron(iii) Oxides. Chem. Mater. 2001, 13, 233–235.

[S3] Kim J., Duck H., Kang K., Lee J. Highly Conformal Deposition of an Ultrathin FeOOH Layer on a Hematite Nanostructure for Efficient Solar Water Splitting. Angewandte Chemie International Edition. 2016, 55, 10854–10858.

[S4] Paracchino, A., Laporte, V., Sivula, K., Grätzel, M. & Timsen, E. Highly Active Oxide Photocathode for Photoelectrochemical Water Reduction. Nat. Mater. 2011, 10, 456–461.

[S5] Zhang Y., Lv H., Zhang Z., Wang L., Wu X., Xu H. Stable Unbiased Photo-Electrochemical Overall Water Splitting Exceeding 3% Efficiency via Covalent Triazine Framework/Metal Oxide Hybrid Photoelectrodes. Adv. Mater. 2021, 33, 2008264.

[S6] Gaulding E. A., Liu G., Chen C. T., Lobbert L., Li A., Segev G., Eichhorn J., Aloni S., Schwartzberg A. M., Sharp I. D., Toma F. M. Fabrication and Optical Characterization of Polystyrene Opal Templates for the Synthesis of Scalable, Nanoporous (Photo)Electrocatalytic Materials by Electrodeposition. J. Mater. Chem. A, 2017, 5, 11601–11614.

[S7] Arunagiri L., Peng Z., Zou X., Yu H., Zhang G., Wang Z., Lai J., Zhang J., Zheng Y., Cui C., Huang F., Zou Y., Wong K., Chow P., Ad H., Yan H. Selective Hole and Electron Transport in Efficient Quaternary Blend Organic Solar Cells. Joule 2020, 4, 1790–1805.

[S8] Kan M., Yang C., Wang Q., Zhang Q., Yan Y., Liu K., Guan A., Zheng G. Defect-Assisted Electron Tunneling for Photoelectrochemical CO_2 Reduction to Ethanol at Low Overpotentials. Adv. Energy Mater. 2022, 12, 2201134.

[S9] Lee K., Lee S., Cho H., Jeong S., Kim W., Lee S., Lee D. Cu^+-incorporated TiO_2 overlayer on Cu_2O nanowire photocathodes for enhanced photoelectrochemical conversion of CO_2 to methanol. Journal of Energy Chemistry. 2018, 27, 264-270.

[S10] Liu G., Zheng F., Li J., Zeng G., Ye Y., Larson D., Yano J., Crumlin E., Ager J., Wang L., Toma F. Investigation and mitigation of degradation mechanisms in Cu_2O photoelectrodes for CO_2 reduction to ethylene. Nature Energy 2021, 6, 1124–1132.

[S11] Deng X., Li R., Wu S., Wang L., Hu J., Ma J., Jiang W., Zhang N., Zheng X., Gao C., Wang L., Zhang Q., Zhu J., Xiong Y. Metal-Organic Framework Coating Enhances the Performance of Cu_2O in Photoelectrochemical CO_2 Reduction. J. Am. Chem. Soc. 2019, 141, 10924–10929.

[S12] Schreier M., Luo J., Gao P., Moehl T., Mayer M., Grätzel M. Covalent Immobilization of a Molecular Catalyst on CuO Photocathodes for CO_2 Reduction. J. Am. Chem. Soc. 2016, 138, 1938–1946.

[S13] Kang H., Nam D., Yang K., Joo W., Kwak H., Kim H., Hong S., Nam K., Joo Y. Synthetic Mechanism Discovery of Mono-Phase Cuprous Oxide for Record High Photoelectrochemical Conversion of CO_2 to Methanol in Water. ACS Nano 2018, 12, 8187–8196.

[S14] Oh S., Kang H., Joo W., Joo Y. Photoelectrochemical CO_2 Reduction via $Cu_2O/CuFeO_2$ Hierarchical nanorods photocatalyst. ChmeCatChem 2020, 12, 5185-5191.

[S15] Zhang Y., Pan D., Tao Y., Shang H., Zhang D., Li G., Li H. Photoelectrocatalytic

Reduction of CO_2 to Syngas via SnO_x-Enhanced Cu_2O Nanowires Photocathodes. Advanced Functional Materials 2022, 32, 2109600.

[S16] Nandal N., Jain S. A Review on Progress and Perspective of Molecular Catalysis in Photoelectrochemical Reduction of CO_2. Coordination Chemistry Reviews. 2022. 451, 214271.

[S17] Arai T., Sato S., Sekizawa K., Suzuki T., Morikawa T. Solar-driven CO_2 to CO Reduction Utilizing H_2O as an Electron Donor by Earth-abundant Mn–bipyridine Complex and Ni-modified Fe-oxyhydroxide Catalysts Activated in a Single-compartment Reactor. Chem. Commun., 2019, 55, 237-240.

[S18] Chen L., Wang Z., Kang P. Efficient Photoelectrocatalytic CO_2 Reduction by Cobalt Complexes at Silicon Electrode. Chinese Journal of Catalysis. 2018, 39, 413-420.

[S19] Leung J., Warnan J., Ly K., Heidary N., Nam D., Kuehnel M., Reisner E. Solar-driven Reduction of Aqueous CO_2 with A Cobalt Bis(terpyridine)-based Photocathode. Nature Catalysis. 2019, 2, 354-365.

[S20] Kou Y., Nakatani S., Sunagawa G., Tachikawa Y., Masui D., Shimada T., Takagi S., Tryk D., Nabetani Y., Tachibana H., Inoue H. Visible Light-induced Reduction of Carbon Dioxide Sensitized by A Porphyrin–rhenium Dyad Metal Complex on p-type Semiconducting NiO as the Reduction Terminal End of An Artificial Photosynthetic System. Journal of Catalysis. 2014, 310, 57-66.

[S21] Wang K, Fan N., Xu B., Wei Z., Chen C., Xie H., Ye W., Peng Y., Shen M., Fan R. Steering the Pathway of Plasmon-Enhanced Photoelectrochemical CO_2 Reduction by Bridging Si and Au Nanoparticles through a TiO_2 Interlayer. Small 2022, 18, 2201882.

[S22] Chu, S.; Ou, P.; Ghamari, P.; Vanka, S.; Zhou, B.; Shih, I.; Song, J.; Mi, Z.

Photoelectrochemical CO_2 reduction into syngas with the metal/oxide interface. J. Am. Chem. Soc. 2018, 140, 7869-7877.

[S23] Liu G., Ye S., Yan P., Xiong F., Fu P., Wang Z., Chen Z., Shi J., Li C. Enabling an Integrated Tantalum Nitride Photoanode to Approach the Theoretical Photocurrent Limit for Solar Water Splitting. Energy Environ. Sci., 2016,9, 1327-1334.